

# Intermittent 3D Diffraction Tomography Combined with In situ Laue Diffraction to Characterize Dislocation Structures and Stress Fields in Microbending Cantilevers

Jean-Baptiste Molin, Loic Renversade, Jean-Sebastien Micha, Olivier Ulrich, Odile Robach, Patric A. Gruber, and Christoph Kirchlechner\*

The mechanisms of plastic deformation are investigated using different characterization tools as scanning electron microscopy (SEM), transmission electron microscopy, or synchrotron-based X-ray techniques like Laue microdiffraction ( $\mu$ Laue). However, structural information can be limited to the specimen surface (SEM), to extremely thin samples (TEM), or depth averaging ( $\mu$ Laue). Until today, a nondestructive in situ investigation of a dislocation population, and de facto, the determination of the local stress tensor in bulk samples, remain challenging. To decompose the depth-integrated  $\mu$ Laue signals, the so-called “differential aperture X-ray microscopy” (DAXM), allowing the 3D determination of the local structural crystal properties, is used. Using this approach, the local crystallographic phase, orientation, and the elastic strain tensor are obtained with  $1 \mu\text{m}^3$  voxel size. In order to accomplish the experiment, a protocol and a new combined in situ mechanical testing rig with a DAXM microscope is created. The experiment is conducted on a severely bent focused ion beam copper single-crystal microcantilever ( $10 \times 10 \times 25 \mu\text{m}^3$ ). The local deviatoric strain tensor and the local lattice curvature in the deformed sample are analyzed in 3D. The advantages and resolution limits of the technique are discussed in detail.


fracture behavior—are governed by the ease of dislocations to move through the crystal lattice.<sup>[1]</sup> Over the past 7 decades, the dislocation behavior has widely been studied via transmission electron microscopy (TEM), which is limited to electron transparent samples. Direct consequences arising from the TEM technique are that only very thin samples can be probed and the obtained data is often not representative for the dislocation arrangement in bulk materials. Until today, a nondestructive in situ investigation of few individual dislocations or a dislocation population within a bulk sample remains challenging. Synchrotron-based Laue microdiffraction ( $\mu$ Laue) is one candidate to probe dislocations at least within micrometer-sized samples. The technique is nondestructive and the lateral resolution has been improving all the time and therefore it is well-suited for the characterization of dislocation structures.<sup>[2–4]</sup>

$\mu$ Laue diffraction patterns (composed of several of so-called Laue peaks) are sensitive to changes of the crystal lattice parameters—namely deviatoric strains—and rotations of the crystallographic unit cell by shifting of the position of Laue peaks.<sup>[5,6]</sup> As the energy of the individual Laue peaks is unknown, only deviatoric strains can be evaluated.<sup>[7]</sup> Dislocations—which cause local strains and rotations of the crystalline lattice—also considerably alter the Laue peak diffraction intensity distribution.<sup>[8,9]</sup> The dislocation content in materials is often divided into two separate subpopulations.<sup>[10,11]</sup> 1) The subset of statistical stored dislocations or “paired dislocations” has the total net-Burger’s vector equaling 0. Only uncorrelated and local lattice distortions are present resulting in an isotropic diffraction peak broadening. 2) The subset of geometrically necessary dislocations (GNDs), also called “unpaired” or “excess” dislocations, with a total net-Burger’s vector is non-zero. GNDs cause an anisotropic diffraction peak broadening in one particular direction which is described hereafter as a peak elongation or peak streaking. If a sample volume is populated with different sets of GNDs one can observe different peak streaking directions and – if only one type of GNDs is assumed – also assess the corresponding GND density and strain gradient.

## 1. Introduction

Mechanical properties of metallic materials—like the yield strength, the strain hardening behavior, or the elastic–plastic

J.-B. Molin, P. A. Gruber, C. Kirchlechner  
Institute for Applied Materials  
Karlsruhe Institute of Technology  
P.O. Box 3640, 76021 Karlsruhe, Germany  
E-mail: kirchlechner@mpie.de, christoph.kirchlechner@kit.edu  
L. Renversade, J.-S. Micha, O. Ulrich, O. Robach  
Université Grenoble Alpes, CEA-Grenoble/Institut de Recherche  
Interdisciplinaire de Grenoble (IRIG)  
Grenoble 38000, France

 The ORCID identification number(s) for the author(s) of this article can be found under <https://doi.org/10.1002/adem.202400357>.

© 2024 The Author(s). Advanced Engineering Materials published by Wiley-VCH GmbH. This is an open access article under the terms of the Creative Commons Attribution-NonCommercial-NoDerivs License, which permits use and distribution in any medium, provided the original work is properly cited, the use is non-commercial and no modifications or adaptations are made.

DOI: 10.1002/adem.202400357

However, the assumption of one GND type is often hampered, particularly, because the  $\mu$ Laue pattern originates from a probed volume whose dimensions are defined by X-ray attenuation length and lateral beam size. In previous works on bent pillars,  $\mu$ Laue patterns exhibited very complicated peak shapes with elongated, curved, and split peaks due to large orientation gradients, elastic distortions, and the formation of subgrains,<sup>[4]</sup> originating from varying GND type and density in the probed volume. Hence, it is often impossible to identify the local GND density and type. To achieve a better interpretation of the 3D GND distribution, we have added an additional aperture to the existing  $\mu$ Laue diffraction setup, which extends the standard  $\mu$ Laue technique. We used the differential aperture X-ray microscopy (DAXM), as it was proposed by Larson et al.<sup>[12]</sup> Using this approach, the local crystallographic phase, orientation, and the elastic strain tensor can be determined with high spatial resolution in 3D.<sup>[13–16]</sup>

In this study we present the application of DAXM for analyzing the evolution of elastic strains and GNDs upon deformation by combining the DAXM setup with an in situ mechanical testing rig. We used this unique instrument to investigate the 3D formation and storage of GND densities and their gradients during microbeam bending. In addition, we analyzed the local deviatoric strain tensor in the deformed sample in 3D.

## 2. Experimental Section

### 2.1. Sample Preparation

The microcantilever was produced via focused ion beam (FIB) milling applying a protocol similar to the one described in refs. [17,18]. For this purpose, rods of  $1 \times 1 \times 15 \text{ mm}^3$  with the length axis parallel to the crystallographic [123] direction were cut from a bulk copper single crystal by electrical discharge machining. The rods were etched to a needle having a cone radius of  $\approx 30 \text{ }\mu\text{m}$  using phosphoric acid ( $\text{H}_3\text{PO}_4$ ). The cantilever was subsequently milled at the top of the needle, to a nominal size of  $9.8 \times 10.2 \times 24.7 \text{ }\mu\text{m}^3$ , using a Zeiss Auriga dual-beam FIB with stepwise reduced currents (coarse milling 4 nA, final

polishing 600pA). It is important to note that the FIB-milled sample can exhibit surface near defects, which typically were limited to a few tens of nanometers beneath the surface.<sup>[19]</sup> Since this concerns only a fraction of a percent of the entire sample volume, it is reasonable to assume that this FIB damage layer is invisible in the standard Laue diffraction patterns.

### 2.2. In situ Laue Microdiffraction (standard $\mu$ Laue)

The experiments were conducted at the CRG-IF beamline (BM32) at the European Synchrotron (ESRF). The beamline setup is described in ref. [6] and is presented in **Figure 1a**. A sub-micrometer ( $0.3 \times 0.3 \text{ }\mu\text{m}^2$ ) polychromatic beam, with a spectral range from 5 to 22 keV, was focused on the sample using two Kirkpatrick Baez mirrors. Above the sample, a Photonic Sciences sCMOS detector having  $2018 \times 2016$  pixels, with a pixel size of  $\approx 73 \text{ }\mu\text{m}$ , was installed at a normal distance of  $\approx 77.1 \text{ mm}$ . Hence,  $\mu$ Laue patterns were recorded in reflection geometry. The Laue pattern acquisition rate was about 3 Hz (accounting for motor speed, detector readout, and exposure time (see **Figure 1a**)). Note that the ideal exposure time varies with peaks spread and therefore with deformation. Here, we optimized the exposure time to the region which was deformed most (weakest Laue peak intensities). Beam stability allowed a large volume area scan, with negligible absolute drift. Detector position and orientation with respect to sample position and incoming beam orientation was calibrated from an unstrained germanium (111) wafer Laue pattern measured before each scan. An optical microscope normal to the sample surface and a fluorescent detector were used to place the sample into the focused beam. The setup was placed on a table with an active vibration and slow inclination drift correction to prevent beam shifts during the experiments.

The mechanical experiment was conducted with an in-house-built displacement-controlled straining rig, designed in accordance with the  $\mu$ Laue setup available at the beamline.<sup>[2]</sup> Different mechanical tests could be performed like tension, compression, bending, and fatigue.<sup>[4,20,21]</sup> The straining rig provided an independent sample and tip alignment with submicrometer

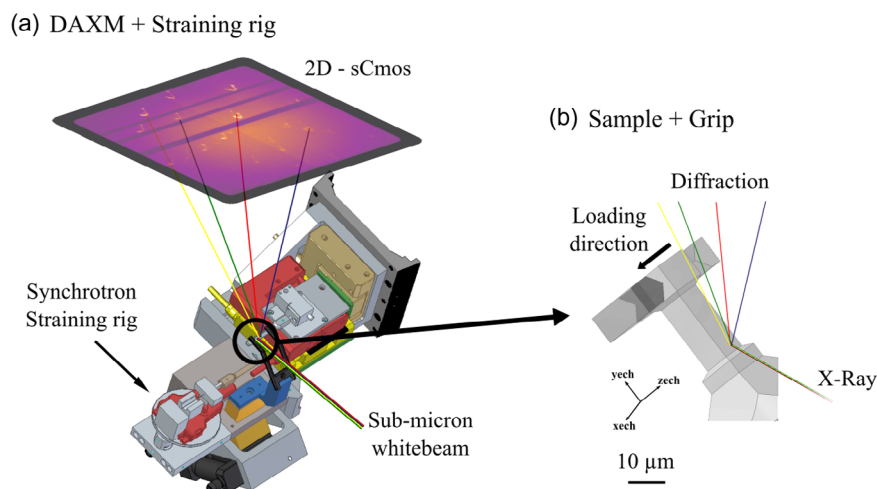


**Figure 1.** Schematic of a) the combination of the DAXM setup together with the mechanical testing rig and b) a magnified view on the microcantilever sample and loading grip.

precision and a displacement range of 32  $\mu\text{m}$ . Simultaneously, the load was measured based on the eigenfrequency of a 30  $\mu\text{m}$ -thick prestrained tungsten wire with a load resolution of 10  $\mu\text{N}$ . To bend the sample, a sample grip produced from a steel razor blade was cut via FIB, similar to refs. [22,23]. The deformation was conducted in a displacement-controlled mode with a constant speed of 10  $\text{nm s}^{-1}$  and a total displacement of 3.5  $\mu\text{m}$ . At the same time, in situ  $\mu\text{Laue}$  patterns were recorded with a frame rate of 2  $\text{s}^{-1}$ . For this purpose, the X-ray beam illuminated a defined area at the first third of the cantilever gauge section, where dislocation activity was generally most pronounced, due to the maximum momentum close to the cantilever fixation, as shown in Figure 1b.

### 2.3. Differential Aperture X-ray Microscopy (DAXM)

As detailed in refs. [24,25] [Larson, 2002 #2], the DAXM principle is based on the knife-edge technique (differential aperture), that records pixel intensity  $S$  as a function of aperture position, as shown in Figure 2a, to allow to determine the local scattering intensity contribution  $I_i$  at voxel  $i$  located at  $y_i$  along the incoming beam path in the sample depth. The voxel size is given by the lateral size of the X-ray beam and wire scan step size. To do so,  $\mu\text{Laue}$  patterns were recorded at different aperture positions  $p_i$  ( $i$  corresponding to the aperture step number,  $i = 1, 2, \dots, N$ ) during an X-ray-absorbing wire scan while keeping a constant sample illumination. The scattering intensity measured at a given detector pixel was composed by all contributions coming from scattering along the X-ray beam path in the sample depth. Assuming a wire with an infinite absorption coefficient, the local scattering intensity  $I_i$  coming from an illuminated region was given by the difference between pixel intensities  $S_i$  and  $S_{i+1}$  corresponding to the wire going from  $p_i$  to  $p_{i+1}$ . Taking into account the shape and a finite absorption coefficient of the wire  $F_{ij}$ , the pixel intensity  $S_i$  and the depth resolved voxel intensity  $I(y)$  can be related by a linear system.

$$S_i = \sum_{j=1}^N F_{ij} I_j \quad (1)$$

The aperture absorption coefficients,  $F_{ij}$ , were deduced from the fit of the aperture transmission profile (Figure 2b).<sup>[26]</sup> For a given detector pixel, the set of scattering intensities  $I_i$  was obtained by solving Equation (1) (by minimization algorithms) at every position  $p_i$ . The  $F_{ij}$  coefficients depend on the distance between the sample and aperture wires, the aperture global design (wire diameter and inclination), wire material absorption coefficient, the sample material absorption coefficient, and the sample thickness. These parameters were refined by a least-square based algorithm from a calibration scan measuring the fluorescence photons coming from the sample during the wire scan using a software called DAXAnalyserGUI being an extension to the main LaueTools software package.<sup>[27]</sup> A comparison between the sample thickness deduced from scanning electron microscopy (SEM) and the refinement is a good indicator of a successful aperture calibration.

We used a multiple wire aperture, composed of four straight tungsten ( $W$ ) wires with a diameter of 50  $\mu\text{m}$ , glued to a copper fork in order to considerably increase the scan speed.<sup>[28]</sup> However, to benefit from multiple wires and reach submicrometer resolution, any overlap of the shadowed regions of the wire must be prevented. Consequently, the wire spacing needs to be large ( $>150 \mu\text{m}$ ) and the wire needs to be close to the sample ( $D_{\text{sCMOS}} \gg D_{\text{ap}}$ ). According to ref. [29], the depth resolution was similar to the aperture step size, under the condition that the aperture moved parallel to the synchrotron beam, that is, horizontally as schematically shown by the arrow in Figure 2a. In the present case, the wire spacing was 500  $\mu\text{m}$  and the aperture was placed 300  $\mu\text{m}$  above the sample surface. To shadow all pixels of the detector, 351 aperture steps with a step size of 1  $\mu\text{m}$  were required. Taking into consideration the lateral resolution given by the submicron beamsizes, the actual voxel size was  $<1 \mu\text{m}^3$ .

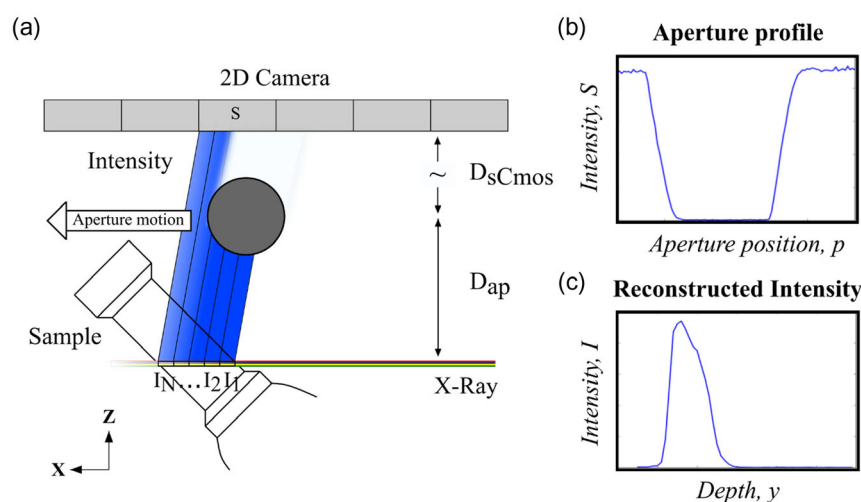


**Figure 2.** a) Schematic of the DAXM principle with  $S$  representing the intensity of one detector pixel being the sum of a set of local scattering intensities  $I_j$  located at voxel  $i$  at depth  $y_i$  along the X-ray beam path. b) Raw data of a Laue pattern 2D camera pixel intensity profile as a function of the aperture position ( $p$ ) showing the full shadow of the scattering intensity originating from the sample. c) Based on the aperture profile and the calibration of aperture trajectory, the depth resolved intensity for a single pixel can be deduced using Equation (1).

## 2.4. Analysis of Reconstructed Laue Patterns

Based on the depth-reconstructed intensities for a number of Laue spots, a standard strain and orientation refinement, with the LaueTools software, can be used to analyze the local dislocation density, lattice strain, and crystallographic orientation. In the present case, the  $\mu$ Laue diffraction patterns were first used to determine the orientation matrix with an accuracy of  $10^{-4}$  radians ( $\approx 6 \times 10^{-3}^\circ$ ), by fitting the peak position of at least eight Laue spots on the detector with 1/10 pixel accuracy. Subsequently, the point-to-point misorientation can be calculated using the following equation.

$$|\theta_{12}| = \min \left( \cos^{-1} \left( \frac{\text{Tr} \left[ (e_i^{\text{cry}} \times g_1) (g_2^T \times e_j^{\text{cry}}) \right] - 1}{2} \right) \right) \quad (2)$$

where  $e^{\text{cry}}$  are the cubic crystal symmetry matrices, and  $g_1$  and  $g_2$  are the orientation matrices of the two points of interest. Then, the first-order kernel average misorientation (nearest-neighborhood kernel average misorientation (KAM)) was calculated.

$$k = \frac{\sum_{i=0}^N |\theta_{1i}|}{N} \quad (3)$$

with  $N$  as the total number of nearest neighbors (i.e., 8, in 2D with square grid). The KAM can be used to deduce the dislocation density  $\rho_{\text{GND}}$ , from ref. [30]

$$\rho_{\text{GND}} = \frac{2\kappa}{b} \quad (4)$$

where  $\kappa$  is the lattice elastic curvature, being the ratio the local misorientation (in rad) divided by the neighbor distance (i.e.  $1 \mu\text{m}$ ) and  $b$  the length of the burgers vector in pure copper ( $2.56 \times 10^{-10} \text{m}$ ).

## 3. Results

### 3.1. How 3D Data Are Represented?

Due to the particular pillar axis direction with respect to the incoming X-ray beam, results are usually displayed in individual planes of interest. As shown on the **Figure 3**, two frames are used to describe our setup: 1) a sample frame described by the orthonormal coordinate system ( $\text{xech}$ ,  $\text{yech}$ ,  $\text{zech}$ ) where  $\text{yech}$  and  $\text{xech}$  are aligned across the sample surface, and  $\text{zech}$  is normal to the sample surface, and 2) a laboratory frame described by ( $X, Y, Z$ ) which is tilted by  $40^\circ$  around the  $\text{xech}$  axis compared to the sample coordinate system. As consequence,  $X$  is aligned with the X-ray beam,  $Y$  is equivalent to  $\text{xech}$ , and  $Z$  points toward the sCmos camera.

As detailed above, voxels are built along the X-ray beam path. A typical 3D dataset is made of an aperture scan performed at each specimen point of a 2D raster scan, with a step size of  $1 \mu\text{m}$  along  $\text{xech}$  and  $2 \mu\text{m}$  along  $\text{yech}$ . The larger step size in  $\text{yech}$  is chosen to account for the  $40^\circ$  inclination of the X-ray beam. Using step size of  $1 \mu\text{m}$  for the aperture scan, which is

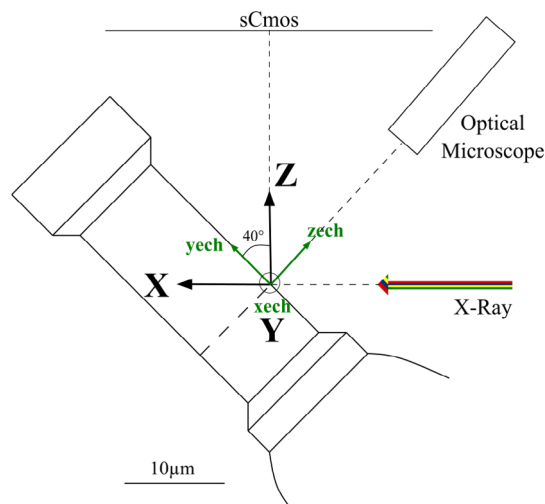


**Figure 3.** Schematic of the two different frames used to analyze and display the results.

along  $X$ , a voxel size of  $\approx 1 \times 1 \times 1 \mu\text{m}^3$  in the ( $X, Y$ ) plane is achieved.

### 3.2. Peak Evolution during In situ Deformation Scans: Standard $\mu$ Laue

Even though all diffraction peaks visible on the detector are recorded simultaneously and also quantitatively interpreted by means of their position and their relative positions on the detector plane providing the orientation matrix and elastic strain of the crystal unit cell, we start our discussion here with the (240) peak (identified after the indexation step). This peak is chosen for the high sensitivity of its shape to GNDs. At early stages of the deformation (primarily during the elastic regime), the peak has a 2D Gaussian shape (circular shape), which proves the crystalline nature of the cantilever without pronounced orientation and strain gradients. Once the plastic regime is reached and dislocation multiplication takes place, the peak shape starts to be elongated (**Figure 4b**). In the underlying case, the integrated Laue pattern shows an elongation in at least two distinct directions, which can be explained by the activation of at least two slip systems. Also one can observe, that a shift of the peak originating from the microcantilever with respect to the 'bulk' peak occurs (**Figure 4b**, white arrow), which indicates a rotation of the cantilever due to bending. The first load drop, which characterizes stress relaxation due to plastic slip in a displacement-controlled experiment, (between (b) and (c) in **Figure 4**) causes peak broadening and elongation and a clear split in the peak shape can be observed (see **Figure 4c**). It attests the plastic character of the deformation. With ongoing deformation, the peak shape gets successively more complex, as shown in **Figure 4d**, exhibiting multiple satellite peaks with an elongated shape. Since the standard Laue analysis is based on a single-crystal model with an internal homogeneous strain distribution, it cannot be applied to noncircular nor asymmetrical Laue peak shape to retrieve unambiguously dislocation-induced orientation and strain gradients in the probed volume.

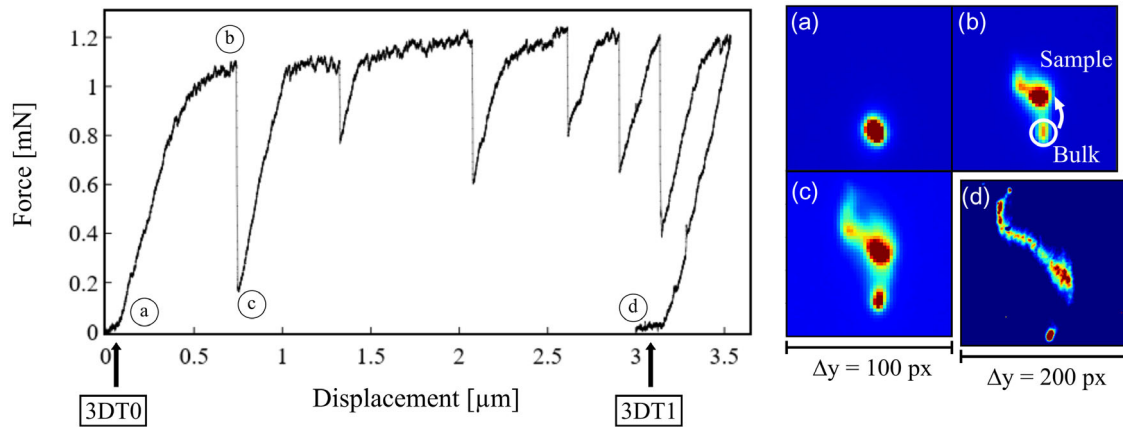


**Figure 4.** Force–displacement curve together with the evolution of the (240) peak shape recorded on the 2D area detector at different deformation states: a) before deformation (circular shape), b) at the onset of the plastic regime (peak shift + small elongation), c) after the first load drop (broadening, elongation + peak splitting), and d) at the end of the bending experiment.

### 3.3. Peak Shape Reconstruction from 3D Volumetric DAXM Scans

To quantitatively understand the peak shape and unveil the 3D distribution of stored GNDs, 3D diffraction tomography (3DT) scans were performed to decompose the peak intensity by depth. Before and subsequent to the bending experiment, two 3DT scans were performed labeled 3DT0 and 3DT1 for the undeformed and deformed state, respectively (Figure 4). To align the 3D tomogram with respect to the highly deformed area in the cantilever we performed a fast 2D raster scan. Subsequently, the 3DT scans were conducted by additional aperture scans in the region of interest (ROI) as defined by the 2D scan. For the 3DT0 scan, a ROI of  $15 \times 18 \mu\text{m}^2$  was chosen. The chosen step sizes were  $1 \mu\text{m}$  along the direction  $x_{\text{ech}}$ , and  $2 \mu\text{m}$  along the direction  $y_{\text{ech}}$ . This led to a final number of 47.250 diffraction patterns being the dataset for the 3D reconstruction. Depending on the exposure time, a 3DT scan took several hours, up to 6 h for a severely deformed sample. Therefore, it was not possible to perform a full 3D reconstruction in situ or in a loaded state, as it was impossible to keep a constant load and strain over such a long period. To determine the depth resolution accuracy of our experiment, we investigate the depth resolved maximum

peak intensity of the (240) Laue spot, recorded at  $6 \mu\text{m}$  from the sample base as shown in Figure 5a. Due to a sample thickness of  $10.2 \mu\text{m}$ , the sample depth along the X-ray beam path (X axis) should be  $15.8 \mu\text{m}$ , resulting from the  $40^\circ$  inclination of the sample with respect to the beam. Based on the depth profile of the maximum peak intensity, as demonstrated in Figure 5b, an experimental depth of  $16 \mu\text{m}$  can be estimated, which is within the aimed depth resolution of  $1 \mu\text{m}$ .

Besides the maximum peak intensity, also the corresponding peak shape is analyzed along the sample depth and is presented in Figure 6. At the upper sample surface ( $0 \mu\text{m}$ ), the peak has one main intensity spot, with low streaking in its surrounding. Deeper in the material ( $1 \mu\text{m}$ ), the scattering intensity is divided in several peaks (hereafter called subpeaks) together with an overall broader streaking, which become more diffuse at larger depth ( $2 \mu\text{m}$ ). A clear discrimination of all the subpeaks becomes difficult, even though three main spots can be deduced. This documents a high density of GNDs and substructure formation with a characteristic length scale well below the  $1 \mu\text{m}$  voxel size in this region. At  $3 \mu\text{m}$  depth, we observed an abrupt change in the streaking direction indicating a change in GND density and type. From this depth on (from 4 to  $8 \mu\text{m}$  depth), multiple subpeaks with similar characteristics (slight broadening but clear peak

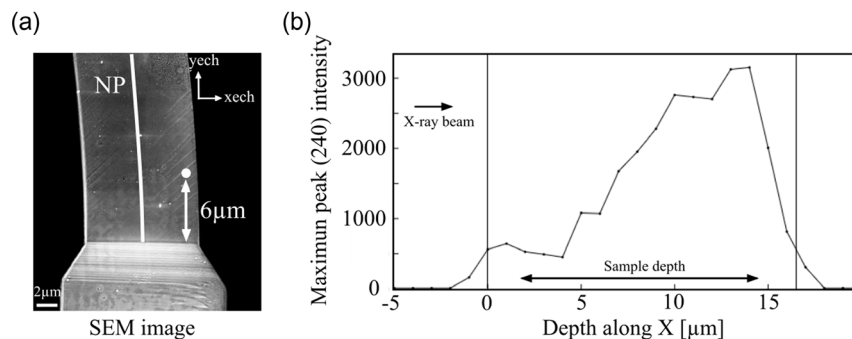


**Figure 5.** a) SEM image of the surface of the deformed microbeam sample (in the  $(x_{\text{ech}}, y_{\text{ech}})$  plane): the white point marks the location of the 3D scan shown here. b) Intensity distribution over depth of the (240) peak after 3D reconstruction.

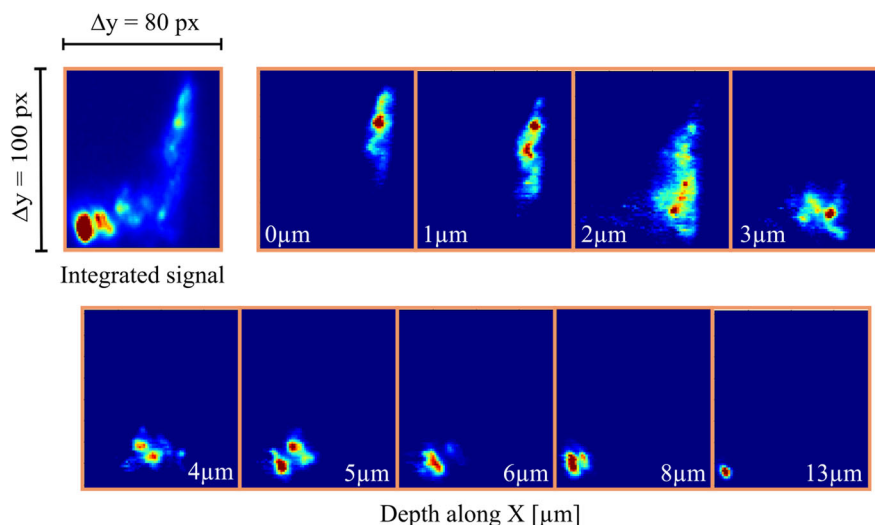


**Figure 6.** Comparison between integrated and depth-resolved scattering intensity around (240) peak. Peak position (mainly due to misorientation) and broadening change over depth.

splitting) appear. From 13 to 16  $\mu\text{m}$ , one remaining peak with a regular circular shape is observed, indicating a negligible storage of GNDs in this region.

### 3.4. Crystal Rotation

From the obtained  $\mu\text{Laue}$  patterns of the 3DT scans, the standard LaueTools software is used for analyzing the depth resolved Laue patterns. The following results, for example, the orientation matrix and strain tensor, are obtained by fitting the main peak intensity positions on the detector.

The bending cantilever experiment exhibits a geometrically predefined rotational axis  $\Theta_{\text{theo}}$ , which is expected to be perpendicular to the applied force and normal to the sample surface, as schematically shown in **Figure 7a**. In ideal bending, only a  $\beta$  rotation (in red) of crystal planes around the axis  $\Theta_{\text{theo}}$  should occur. However, due to the presence of dislocations at the micrometer scale as well as due to possible misalignments, the observed rotation axis might deviate from the ideal one. Using the 3D depth-resolved data we additionally analyze the deviation from the assumed  $\Theta_{\text{theo}}$ , that is, the angle  $\alpha$  (in green) between the assumed rotation axis  $\Theta_{\text{theo}}$  and the actual axis  $\Theta_{\text{exp}}$ . In **Figure 7b,c**, 2D maps of the angle  $\alpha$  within horizontal cross sections of the cantilever (X-Y-plane) for two different sample heights (different *ye*) are presented. The plastically deformed part of the sample, that is, the region at the sample bottom shows significant deviations from the intended rotation axis. While the compressive side of the bending cantilever shows small (or even negligible) deviations (see **Figure 7c**), the tension side (right) of the microbeam exhibits considerable deviations of up to  $3^\circ$ . In the upper section of the cantilever ( $6\ \mu\text{m}$  from sample base, **Figure 7b**)  $\alpha$  is generally lower and shows a maximum of only  $1^\circ$ . The tension compression asymmetry only exists at the lower edge of this section. Possible origins of this phenomenon will be discussed later.

### 3.5. KAM: Local GND Density

A KAM analysis is of interest to localize and determine the GND density distribution within a sample. As shown in **Figure 8**, the (X,Y) plane located  $6\ \mu\text{m}$  above the sample base exhibits a maximum KAM of  $0.042^\circ$  (**Figure 8a**) and  $0.638^\circ$  (**Figure 8b**) for the undeformed and deformed state, respectively. Using Equation (4), this results in a maximum GND density of  $8.16 \times 10^{13}\ \text{m}^{-2}$ , for the highest deformed region of this plane. We observe that the GNDs are not homogeneously distributed and are localized in the plastic zone of the cantilever. A strong localization near the free sample surface with a drop in the GND density toward the neutral plane is observed. A mosaic image of the scattering intensity distribution around the (240) diffraction peak is presented in **Figure 8c** for comparison. It shows the strongest peak streaking in the region of the highest KAM. The comparison with the exemplary integrated (240) diffraction peaks at the bottom of **Figure 8c** clearly shows, that without DAXM, the peak shape in the plastically deformed regions is much more complex and cannot be analyzed, and quantitative analysis is only possible with DAXM.

The KAM analysis can also be applied for the 3D reconstruction of the entire scanned sample. Using a new home-developed interactive interface, called LaueDisplayTomogram, the handling and visualization of a full 3D sample are possible, as shown on the **Figure 9**. Considering the entire scanned undeformed sample, a maximum KAM value of  $0.07^\circ$  is observed and the sample exhibits an average KAM of  $1.5 \times 10^{-2\circ} \pm 10^{-3\circ}$ . Therefore, the GND density is of the order of  $10^{12}\ \text{m}^{-2}$ —using Equation (4)—confirming that the sample exhibits a low number of GNDs with respect to the total dislocation density of about  $\approx 10^{13}\ \text{m}^{-2}$  of the annealed Cu sample before mechanical testing. In contrast, the average KAM of the bent cantilever is  $4.53 \times 10^{-1\circ} \pm 10^{-3\circ}$ , which is 30 times higher than in the undeformed sample. With a maximum KAM value of  $1^\circ$  in **Figure 9**,

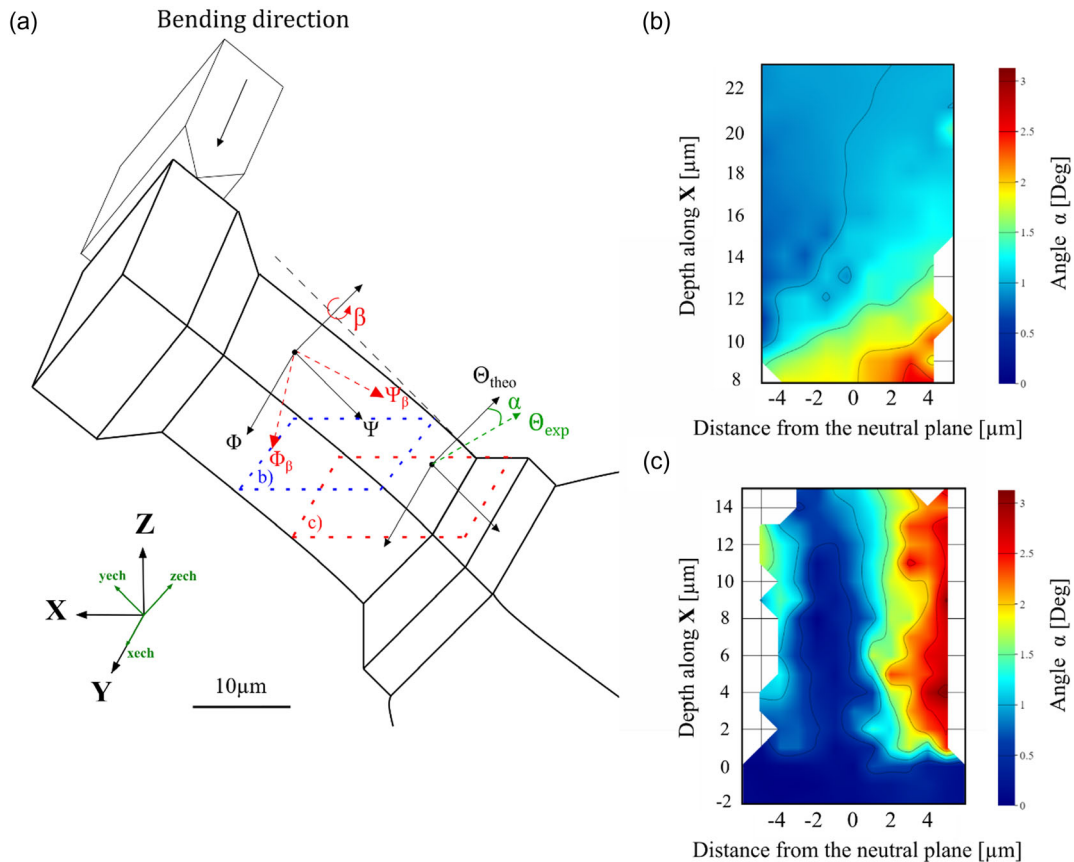


**Figure 7.** Analysis of expected and unexpected sample rotations. a) Schematic of the expected rotation angle  $\beta$  for pure bending and the unexpected misalignment angle  $\alpha$  between the theoretical rotation axis  $\Theta_{theo}$  and the real rotation axis  $\Theta_{exp}$ . 2D maps of the local misalignment angle  $\alpha$  for (X,Y) planes located b) 6  $\mu\text{m}$  above the sample base (blue dotted plane) and c) at the sample base (red dotted plane).

the maximum GND density in the deformed sample is  $1.32 \times 10^{14} \text{ m}^{-2}$ .

As expected, the maximum values for the KAM and GND densities are localized within the first micrometer of the gauge length, where also a large number of slip traces is found in the SEM image.

### 3.6. Deviatoric Strain Tensor

Despite the successful reconstruction of the 3D KAM distribution, an analysis of the 3D deviatoric strain distribution with sufficiently high accuracy remains challenging. As shown in Figure 5, the applied spatial resolution (voxel size) does not permit to fully separate all subpeaks in severely deformed regions. This renders a fully automatized strain refinement difficult and requires a manual supervision of the peak identification processes. For unsupervised image interpretation, a further increase in spatial resolution would be necessary to minimize the number of subpeaks and allow a fully automatized strain refinement in the entire sample. Hence, for a successful experiment including strain analysis, an optimum balance between the depth

resolution limit and the applied deformation should be estimated and met.

In the present study, at least for small deformations such as present close to the neutral plane and distant from the highly deformed area, that is, at the sample bottom (Figure 8), where either no subpeaks or well-defined subpeaks occur, the elastic deviatoric strain tensor can be deduced. An example for the strain measurement of an unloaded but deformed microcantilever is presented in Figure 10, where the elastic strain along the cantilever axis  $\epsilon_{xx}$  is shown.

First, zero strain can be observed at the neutral plane (white dashed line) and a compressive and a tensile strain is found on the outer fibers. This is expected for an unloaded cantilever which was symmetrically deformed in pure bending.

However, starting at around 6  $\mu\text{m}$  depth along X, a visible strain asymmetry across the neutral plane appears, where the strains at the outer fibers start to decrease and some tensile strain along the neutral fiber evolves. This observation can also be correlated to the asymmetric peak broadening observable on the mosaic image (Figure 8). Here, at similar depth along X, some peak streaking is only observed on the compressive side, while on the tension side no peak elongation is found.

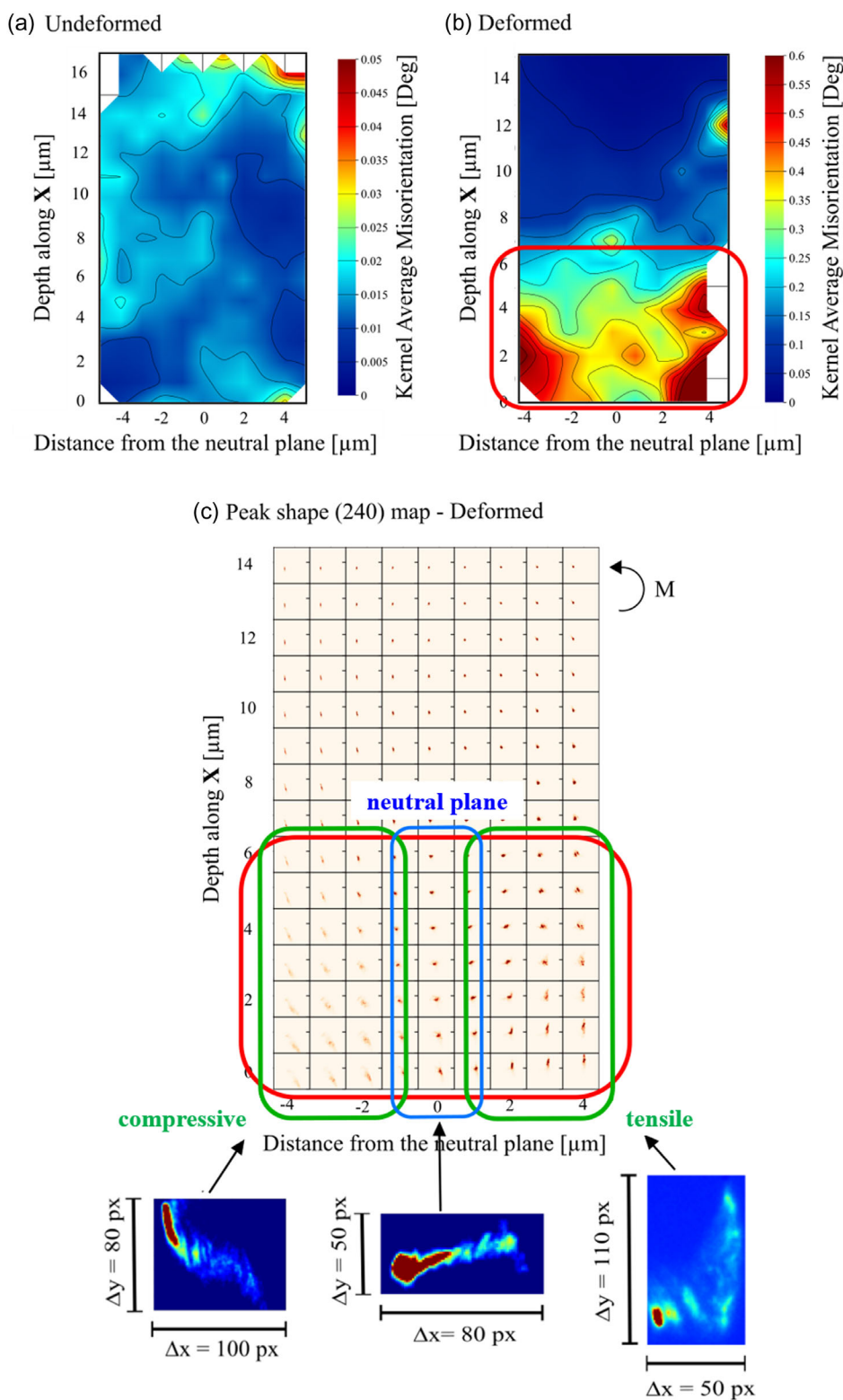


**Figure 8.** For the (X, Y) plane located 6  $\mu\text{m}$  above the sample base: 2D maps of the KAM for a) the undeformed state (scan 3DT0) and b) the deformed state (scan 3DT1). c) 2D map of the scattering intensity around the (240) diffraction peak in the deformed state together with exemplary integrated (240) Laue diffraction peaks for the compressive side, neutral plane, and tensile side, respectively.



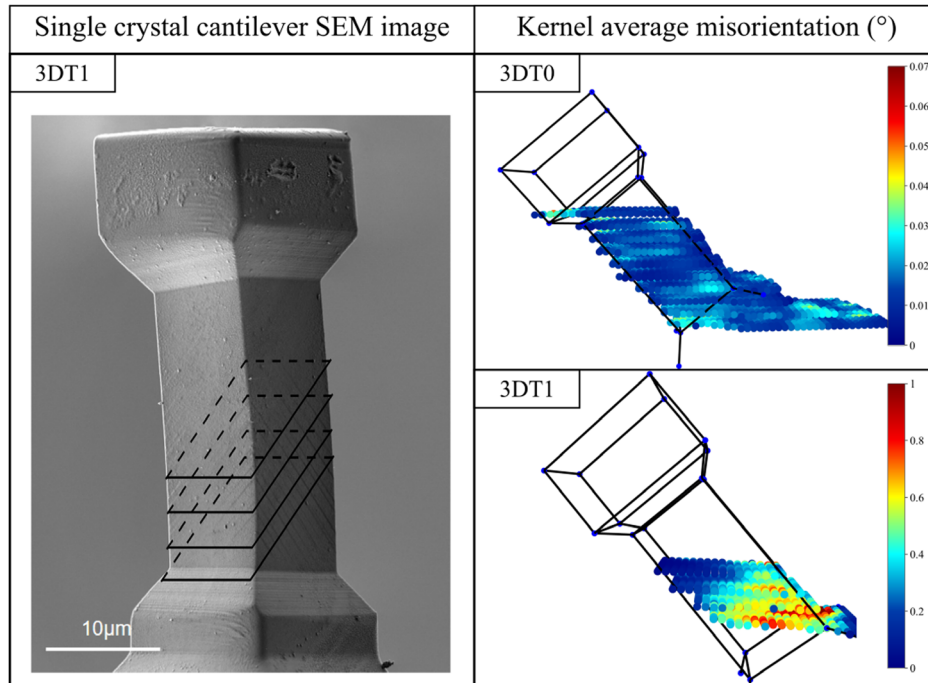


**Figure 9.** 3D DT of an undeformed and bent single-crystal cantilever. Deformation is localized at the sample bottom as documented by a huge number of slip steps in the SEM image (left) and the increased KAM values in the 3D representation of the first-order KAM of the undeformed and deformed sample (right).

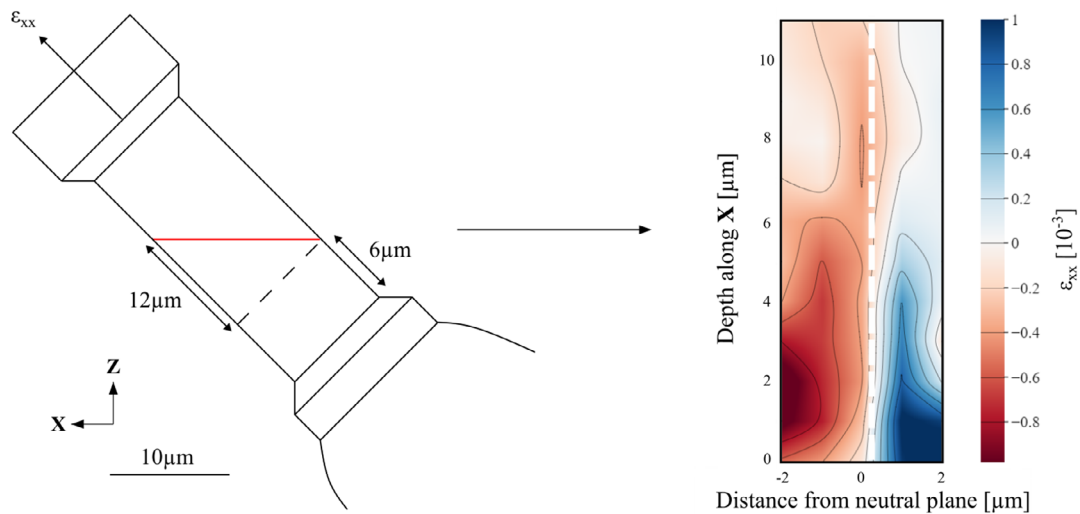


**Figure 10.** 2D map of the elastic strain  $\epsilon_{xx}$  along the cantilever axis near the neutral plane. The location of the investigated sample plane is shown in the schematic on the left in red.

## 4. Discussion

### 4.1. Resolution and Advantages of 3D $\mu$ Laue Diffraction

The lateral resolution of  $\mu$ Laue diffraction is determined by the synchrotron beam size, which depends on the beamline optics and source size. A resolution of  $0.3 \times 0.3 \mu\text{m}^2$  (Y, Z) is routinely achievable. In contrast, along X the depth, resolution limits

depend on the step size between each recorded pattern, which is given by the step size resolution of the motors for the lateral translation of the aperture. In our setup, the minimum step size is 300 nm, actually 3.3 times smaller than the  $1 \mu\text{m}$  used in the work presented here. Hence, high-resolution 3DT with a  $0.3 \times 0.3 \times 0.3 \mu\text{m}^3$  sized voxel would theoretically be possible. However, the real resolution strongly depends on the setup and alignment of the aperture which itself depends on several

experimental parameters, namely, the material it is made of, its geometry, and last but not least its position with respect to sample surface. As an example, the aperture must be positioned with less than 500  $\mu\text{m}$  distance from the sample surface and still moved without any collision with other parts of the sample holder to reach a resolution below 1  $\mu\text{m}$ .<sup>[28]</sup> This is not easily achievable in all environments, especially if the DAXM setup shall be combined with in situ testing devices.

Besides the spatial resolution, the required time to perform specific scans is of utmost importance. A 3.5 Hz pattern acquisition frequency, as it was used in the present work, is sufficient to perform intermittent 2D Laue diffraction scans even during in situ mechanical experiments using a displacement-controlled setup. On the contrary, the time required for a 3DT scan, aiming for 1  $\mu\text{m}^3$  voxel size and using the same frame rate, is around 6 h, which is too long for “in situ” imaging, as load and/or displacement cannot be maintained constant for such a long time.

The 3D reconstruction of the peak intensity, that is, the depth decomposition of the peak, reduces the complexity of a streaked 2D Laue spot considerably and makes it more interpretable as originating from a single homogeneous crystal. After reconstruction, each subpeak may correspond to a smaller volume with less internal strain heterogeneities and average elastic strain components values can be obtained by the standard single-crystal strain and orientation refinement step. This is a twofold advantage, as the strain and KAM analysis are possible at all, and on top, the third dimension can be explored. The strain map in Figure 10 acts as impressive example of the local strain resolution. Even more, in addition to the strain evaluation, the 3D GND density distribution within a deformed sample (e.g., Figure 8) or the exact location of a subgrain or a dislocation pile-up can be determined (e.g., Figure 6).

#### 4.2. What Can We Learn from 3D Data Regarding the Dislocation Behavior in a Deformed Microcantilever?

Now, we want to shed light on the unexpected rotational axis of the Cu crystal as well its variation across the sample (Figure 7). The discrepancy of the observed rotation axis with respect to the ideal rotation axis could be explained by two effects: 1) an experimental misalignment between the grip (tip), and the sample, leading to an unwanted sample twist; or 2) the storage of a subset of GNDs, which leads to an additional strain gradient with a different orientation compared to the strain gradient from pure bending.

In a misaligned sample, we would assume that the entire cantilever is bent homogeneously and the misorientation angle would be constant along the sample. However, in our case, we observe a strong variation of the crystallographic rotation axes within the sample which requires a local variation of stored GNDs. To explain the strong tension–compression asymmetry in our sample we shall consider the shear stress acting on dislocations on either side of the neutral plane. In case of finite beam bending with a fixed end, the stress tensor acting on a subvolume  $\sigma_{\text{tot}}$  is the summation of the bending stress  $\sigma_{\text{bend}}$  and the shear stress  $\tau_{\text{shear}}$ . Considering the pure Euler–Bernoulli bending beam theory,  $\sigma_{\text{bend}}$  has one component  $\sigma_{xx}$  in the sample frame (along the cantilever axis), with a different sign in the tensile or compressive

region of the cantilever. The bending stress scales linearly with the distance from the neutral plane, at least in the purely elastic case, which we consider here for simplicity.  $\tau_{\text{shear}}$  depends on the loading direction and can, due to the symmetry of the stress tensor, be written as  $\tau_{\text{shear}} = \tau_{xy} = \tau_{yx}$ . Therefore,  $\sigma_{\text{tot}}$  has the following form.

$$\sigma_{\text{tot}} = \begin{pmatrix} \pm\sigma_{xx} & \tau_{xy} & 0 \\ \tau_{xy} & 0 & 0 \\ 0 & 0 & 0 \end{pmatrix} \quad (5)$$

With

$$\sigma_{xx,\text{max}} = 4 \frac{F_{\text{max}} L}{t^2 b} \quad \text{and} \quad \tau_{xy,\text{max}} = \frac{3 F_{\text{max}}}{2 b t} \quad (6)$$

$F_{\text{max}}$  is the maximum applied force in the elastic region.  $L$ ,  $b$ , and  $t$  are the length (where the force is applied), the width, and the thickness of the cantilever, respectively. The given terms for  $\sigma_{xx,\text{max}}$  and  $\tau_{xy,\text{max}}$  yield the maximum values for  $\sigma_{xx}$  and  $\tau_{xy}$  within the cross section of the cantilever. Please note that  $\sigma_{xx}$  is maximal at the outmost fibers of the cantilever while  $\tau_{xy}$  is maximal within the neutral plane.  $\tau_{xy}$  also decreases parabolically to zero from the neutral plane to the outmost fibers of the cantilever.

A uniaxial Schmid factor calculation cannot be used for assessing the shear stress acting on an individual dislocation; hence, we use the orientation tensor  $m^s$ , as detailed in ref. [31], which is determined by the outer product between the slip plane  $l^s$  and normal direction  $n^s$ , in the sample frame.

$$m^s = \frac{1}{2} (l^s \otimes n^s + n^s \otimes l^s) \quad (7)$$

Using Equation (5) and (7), we can determine the Schmid factor  $m$ .

$$\sigma : m^s = \sigma_{xx} m \quad (8)$$

Often, the effect of the global shear stress can be neglected, and the experiment can be considered as pure bending. However, the shear stress cannot be neglected in any case. Based on Equation (8), the Schmid factor has the following form.

$$m = \left| 2 \frac{\tau_{xy}}{\sigma_{xx}} m_{12}^s \pm m_{11}^s \right| \quad (9)$$

Consequently, due to the change in sign of the bending stress (the  $\sigma_{xx}$  component), the resolved shear stress and the Schmid factor are different for the compression and tension side of the microcantilever.

In the underlying case of our bending cantilever, we focus our discussion on the asymmetry of the Schmid factor on the two slip systems with the highest resolved shear stress as listed in Table 1. The calculation of the Schmid factors was done at the fixed end of the cantilever (see Figure 7c), where the global contribution of the nonzero macroscopic shear stress to the resolved shear stress on a slip system is below 10% for the given length and thickness of the cantilever. On the compression side, the primary slip system with the highest Schmid factor is identified as the (111)[–101]. It is expected to be activated first. The secondary slip

**Table 1.** Calculated Schmid factors  $m$  considering a global shear stress  $\tau_{xy}$  for the two slip systems SS with the highest Schmid factor and for the compression as well as the tension side of the cantilever.

$\tau_{xy} = 0$ MPa		$\tau_{xy} = 17$ MPa (10% of $\sigma_{xx}$ )			
Compression/Tension		Compression		Tension	
$m$	SS	$m$	SS	$m$	SS
0.416	(111)[−101]	0.413	(111)[−101]	0.432	(111)[−110]
0.405	(111)[−110]	0.363	(111)[−110]	0.398	(111)[−101]

system, with the second highest Schmid factor is (111)[−110]. Irrespective of global shear stresses, the order of primary and secondary slip systems does not change. On the tensile side of the bending cantilever, however, the Schmid factor of the former secondary slip system increases with increasing global shear stress and becomes larger than the Schmid factor of the initial primary slip system. Hence, considering the global shear stress, we expect the activation of two different subsets of dislocations with different Burger's vectors on the compression and tension side of the cantilever. The observation of the localized misalignment of the rotation axis with respect to the rotation axis of pure bending in the plastically deformed region of the tensile side of the cantilever (see Figure 7b,c) is consistent with the consideration of the different activated slip systems. Without the 3D ability of the introduced experimental approach, we would not be able to see and analyze these minor and localized changes.

## 5. Conclusion

Here we have demonstrated the first nondestructive intermitted 3D investigation of a bent Cu micro cantilever using DAXM. The actual resolution of  $1 \times 1 \times 1 \mu\text{m}^3$  proved to be sufficient to realize novel aspects and more details of the deformation behavior of a metallic microcantilever. We were able to quantify the elastic strain fields, the local distribution of KAM, and the corresponding storage of GNDs to localize subgrain boundaries within the micro cantilever. Unexpected asymmetries in the elastic strain field and unexpected local misalignments of crystal rotation axes could be explained by a modified Schmid factor analysis considering the influence of a global shear stress and the locally different activation of different subsets of slip systems on the tension and compression side of the microcantilever. A further increase of the resolution (smaller voxel size) would ease the automatic deviatoric strain tensor analysis in this severely bent sample, even though it might already be sufficient for standard micropillars or grains in polycrystalline materials. The combined DAXM, in situ deformation setup, offers unique possibilities to study dislocation-based phenomena at the micrometer scale.

## Acknowledgements

The author thanks the BM32 team for their assistance and knowledge during the X-Ray experiment. The European Synchrotron Facility is gratefully acknowledged for beamtime allocation at the French beamline BM32-CRG\_IF. Moreover, the authors acknowledge the funding provided

by the ANR-DFG within the XmicroFatigue project (DFG project number 316662945).

## Conflict of Interest

The authors declare no conflict of interest.

## Data Availability Statement

The data that support the findings of this study are available from the corresponding author upon reasonable request.

## Keywords

differential aperture X-ray microscopy, dislocation pile-up, small-scale mechanical testing, stress fields

Received: February 12, 2024

Revised: June 6, 2024

Published online:

- [1] G. Dehm, *Prog. Mater. Sci.* **2009**, *54*, 664.
- [2] C. Kirchlechner, J. Keckes, J. S. Micha, G. Dehm, *Neutrons and Synchrotron Radiation in Engineering Materials Science: From Fundamentals to Applications*, Wiley-VCH Verlag GmbH & Co KGaA **2017**, pp. 425–438.
- [3] A. Davydok, B. N. Jaya, O. Robach, O. Ulrich, J.-S. Micha, C. Kirchlechner, *Mater. Des.* **2016**, *108*, 68.
- [4] C. Kirchlechner, W. Grosinger, M. Kapp, P. Imrich, J.-S. Micha, O. Ulrich, J. Keckes, G. Dehm, C. Motz, *Philos. Mag.* **2012**, *92*, 3231.
- [5] N. Tamura, R. Celestre, A. MacDowell, H. Padmore, R. Spolenak, B. Valek, N. Meier Chang, A. Manceau, J. Patel, *Rev. Sci. Instrum.* **2002**, *73*, 1369.
- [6] O. Ulrich, X. Biquard, P. Bleuet, O. Geaymond, P. Gergaud, J. Micha, O. Robach, F. Rieutord, *Rev. Sci. Instrum.* **2011**, *82*, 033908.
- [7] J.-S. Chung, G. E. Ice, *J. Appl. Phys.* **1999**, *86*, 5249.
- [8] J. Zimmermann, S. Van Petegem, H. Bei, D. Grolimund, E. P. George, H. Van Swygenhoven, *Scr. Mater.* **2010**, *62*, 746.
- [9] C. Marichal, K. Srivastava, D. Weygand, S. Van Petegem, D. Grolimund, P. Gumbsch, H. Van Swygenhoven, *Phys. Rev. Lett.* **2014**, *113*, 025501.
- [10] J. F. Nye, *Acta Metall.* **1953**, *1*, 153.
- [11] M. Ashby, *Philos. Mag.* **1970**, *21*, 399.
- [12] B. Larson, W. Yang, G. Ice, J. Budai, J. Tischler, *Nature* **2002**, *415*, 887.
- [13] O. M. Barabash, M. Santella, R. I. Barabash, G. E. Ice, J. Tischler, *JOM* **2010**, *62*, 29.
- [14] Y. Guo, D. Collins, E. Tarleton, F. Hofmann, J. Tischler, W. Liu, R. Xu, A. Wilkinson, T. Britton, *Acta Mater.* **2015**, *96*, 229.
- [15] R. Li, Q. Xie, Y.-D. Wang, W. Liu, M. Wang, G. Wu, X. Li, M. Zhang, Z. Lu, C. Geng, *Proc. Natl. Acad. Sci.* **2018**, *115*, 483.
- [16] Y. Guo, D. M. Collins, E. Tarleton, F. Hofmann, A. J. Wilkinson, T. B. Britton, *Acta Mater.* **2020**, *182*, 172.
- [17] C. Motz, T. Schöberl, R. Pippan, *Acta Mater.* **2005**, *53*, 4269.
- [18] D. Kiener, W. Grosinger, G. Dehm, R. Pippan, *Acta Mater.* **2008**, *56*, 580.
- [19] D. Kiener, C. Motz, M. Rester, M. Jenko, G. Dehm, *Mater. Sci. Eng., A* **2007**, *459*, 262.
- [20] C. Kirchlechner, P. Imrich, W. Grosinger, M. Kapp, J. Keckes, J.-S. Micha, O. Ulrich, O. Thomas, S. Labat, C. Motz, *Acta Mater.* **2012**, *60*, 1252.

- [21] N. Malyar, J.-S. Micha, G. Dehm, C. Kirchlechner, *Acta Mater.* **2017**, 129, 91.
- [22] C. Kirchlechner, P. J. Imrich, W. Liegl, J. Pörnbacher, J.-S. Micha, O. Ulrich, C. Motz, *Acta Mater.* **2015**, 94, 69.
- [23] D. Kiener, C. Motz, W. Grosinger, D. Weygand, R. Pippan, *Scr. Mater.* **2010**, 63, 500.
- [24] B. Larson, W. Yang, J. Tischler, G. Ice, J. Budai, W. Liu, H. Weiland, *Int. J. Plast.* **2004**, 20, 543.
- [25] G. E. Ice, J. W. Pang, *Mater. Charact.* **2009**, 60, 1191.
- [26] L. Renversade, J. B. Molin, O. Robach, S. Tardif, O. Ulrich, C. Kirchlechner, J.-S. Micha, *Depth-Resolved Laue Patterns By 3D Laue Microdiffraction On CRG-IF BM32 Beamline at ESRF* (in Preparation).
- [27] J.-S. Micha, O. Robach, S. Tardif, *LaueTools Open Source Python Packages for X-ray MicroLaue Diffraction Analysis* **2024**.
- [28] J.-S. Chung, S. Isa, V. Greene, O. Broadwater, W. Liu, G. E. Ice, *Nucl. Instrum. Methods Phys. Res., Sect. A* **2007**, 582, 212.
- [29] J.-B. Marijon, *PhD Thesis, Jean-Baptiste Marijon*École doctorale Sciences des métiers de l'ingénieur, (Paris) **2017**.
- [30] H. Gao, Y. Huang, W. Nix, J. Hutchinson, *J. Mech. Phys. Solids* **1999**, 47, 1239.
- [31] E. C. Aifantis, *Mater. Sci. Eng.* **1986**, 81, 563.